Geomech. Geophys. Geo-energ. Geo-resour. (2016) 2:63–76
DOI 10.1007/s40948-016-0022-6

ORIGINAL ARTICLE

Breakdown pressure and fracture surface morphology of hydraulic fracturing in shale with H_2O, CO_2 and N_2

Xiang Li · Zijun Feng · Gang Han · Derek Elsworth · Chris Marone · Demian Saffer · Dae-Sung Cheon

Received: 3 November 2015 / Accepted: 15 December 2015 / Published online: 26 January 2016
© Springer International Publishing Switzerland 2016

Abstract Slick-water fracturing is the most routine form of well stimulation in shales; however N_2, LPG and CO_2 have all been used as "exotic" stimulants in various hydrocarbon reservoirs. We explore the use of these gases as stimulants on Green River shale to compare the form and behavior of fractures in shale driven by different gas compositions and states and indexed by breakdown pressure and the resulting morphology of the fracture networks. Fracturing is completed on cylindrical samples containing a single blind axial borehole under simple triaxial conditions with confining pressure ranging from 10 to 25 MPa and axial stress ranging from 0 to 35 MPa ($\sigma_1 > \sigma_2 = \sigma_3$). Results show that: (1) under the same stress conditions, CO_2 returns the highest breakdown pressure, followed by N_2, and with H_2O exhibiting the lowest breakdown pressure; (2) CO_2 fracturing, compared to other fracturing fluids, creates nominally the most complex fracturing patterns as well as the roughest fracture surface and with the greatest apparent local damage followed by H_2O and then N_2; (3) under conditions of constant injection rate, the CO_2 pressure build-up record exhibits condensation between $\sim$5 and 7 MPa and transits from gas to liquid through a mixed-phase region rather than directly to liquid as for H_2O and N_2 which do not; (4) there is a positive correlation between minimum principal stress and breakdown pressure for failure both by transverse fracturing (σ_3 *axial*) and by longitudinal fracturing (σ_3 *radial*) for each fracturing fluid with CO_2 having the highest correlation coefficient/slope and lowest for H_2O. We explain these results in terms of a mechanistic understanding of breakdown, and through correlations with the specific properties of the stimulating fluids.

Keywords Green River Shale · Hydraulic fracturing · Breakdown pressure · Fracture roughness · Fracture complexity · Fractal dimension

X. Li (✉) · Z. Feng · D. Elsworth
John and Willie Leone Family Department of Energy and Mineral Engineering, EMS Energy Institute and G3 Center, The Pennsylvania State University, University Park, PA 16802, USA
e-mail: xzl111@psu.edu

Z. Feng
Department of Mining Engineering, Taiyuan University of Technology, Taiyuan 030024, Shanxi, China

G. Han
Aramco Services Company, Houston, TX 77096, USA

D. Elsworth · C. Marone · D. Saffer
Department of Geosciences, EMS Energy Institute and G3 Center, The Pennsylvania State University, University Park, PA 16802, USA

D.-S. Cheon
Geologic Environment Division, Underground Space Department, KIGAM, Daejeon 305-350, Korea

1 Introduction

Hydraulic fracturing is a mature completion technique which has been extensively applied in tight and unconventional gas reservoirs. For unconventional reservoirs such as shale with extremely low permeability, long horizontal laterals with multi-staged hydraulic fractures are necessary to deliver economic production. The introduction of hydraulic fractures significantly increases flow rate because of large surface contact area between fractures and the reservoir, enhanced permeability around the wellbore, and reduced fluid diffusion lengths (King 2010; Vincent 2010; Faraj and Brown 2010).

Water-based fluids have become the predominant type of fracturing fluid. Sometimes N_2 or CO_2 gas is combined with the fracturing fluids to form foam as the base fluid. Other additives can also be combined with N_2 or CO_2 to improve the efficiency, e.g. coupling solids-free viscoelastic surfactants (VES) with a carbon dioxide (CO_2)-emulsified system to further enhance cleanup in a depleted reservoir, extend the application to water-sensitive formations, and maintain reservoir gas saturation to prevent any potential water blockage (Hall et al. 2005); or incorporating low-polymer-loading carboxymethyl guar polymer and a zirconium-based crosslinker to minimize the damage and maximize production (Gupta et al. 2009). For unconventional reservoirs in arid areas the availability of water is sparse. In these cases, N_2, liquefied petroleum gas (LPG) or CO_2 may become an "exotic" option for stimulation fluid. For example, fracturing with CO_2 has been used in places such as Wyoming where carbon dioxide supply and infrastructure are available (Bullis 2013).

Using CO_2 or N_2 as stimulation fluid has a number of potential advantages. Not only can it eliminate the need for large volume of water—approximately 5 million gallons per treatment—but it can also reduce the amount of wastewater produced and therefore reduce the need for re-injection, which is known to induce seismicity in some cases (Weingarten et al. 2015) and the environmental footprint of these operations. Energized fluids with a gas component can facilitate gas flowback in tight, depleted or water sensitive formations and may be required when drawdown pressures are smaller than the capillary forces in the formation (Friehauf and Sharma 2009; Friehauf 2009). Some recent studies suggest that using carbon dioxide can also result in a more extensive and interconnected network of fractures, making it easier to extract the resource (Ishida et al. 2012). Other work argues that fractures created with N_2 are more complex than CO_2 which in turn are more complex than those formed by H_2O, where fracture pattern complexity is based on the ratio of fracture surface area to rock volume, with rough, intricate fracture having high complexity and greater potential to access pore space in tight shales and other formations (Alpern et al. 2013; Gan et al. 2013).

Classic geomechanics models suggest that breakdown pressure is independent of fluid type (composition) or state (gas or liquid) in that failure is controlled by effective stress, alone for a given rock tensile strength (Hubbert and Willis 1957; Biot 1941; Haimson and Fairhurst 1967). However recent research suggests that fluid composition and/or state may have great influence on breakdown pressure (Alpern et al. 2012; Gan et al.2013). The purpose of this study is to explore the development and behavior of fractures in Green River Shale (GRS) when injected with H_2O, CO_2 and N_2. We focus in particular on breakdown pressure and fracture morphology, including fracture surface roughness and the complexity of the resulting fracture network.

2 Experimental method

The introduction and behavior of induced fractures in shale by H_2O, CO_2 and N_2 are investigated with respect to breakdown pressures and morphology of the resulting fracture networks. These experiments are conducted on Green River shale.

2.1 Approach

Hydraulic fracturing experiments are conducted using intact cylindrical cores containing a blind central borehole ($\sim$1/10-inch-diameter to depth of 1-inch). These experiments measure breakdown pressure and examine the morphology of the resulting fracture. Cores are 1-inch diameter and 2-inches long, sheathed in a jacket, and subjected to mean and deviatoric stresses in a simple triaxial configuration. Multiple cores of GRS are tested with H_2O, CO_2 and N_2. Post-experiment fracture surfaces are measured using a

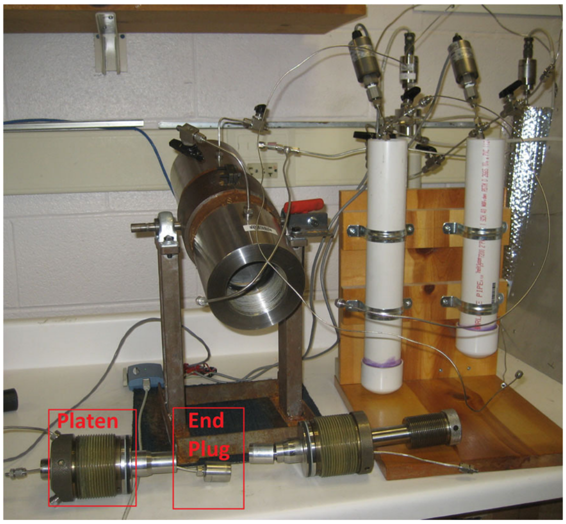

Fig. 1 Hydraulic fracturing system. Containment vessel with platen and fluid feed assembly and cell end-caps in foreground

Zygo NewView 7300 scanning white light interferometer for surface roughness and complexity.

2.2 Apparatus

All experiments in this study are completed using a standard triaxial apparatus configured for hydraulic fracturing as shown in Figs. 1 and 2. The triaxial core holder (Temco) accommodates the membrane-sheathed cylindrical samples (1-inch diameter and 2-inches long) and applies independent loading in the radial and axial directions via syringe pumps.

2.3 Sample design and seal method

Green River shale samples with a diameter of 1-inch are trimmed by saw to a length of 2-inches and then end-grounded. A central borehole (1/10-inch-diameter) is drilled to a depth of 1-inch (Fig. 3).

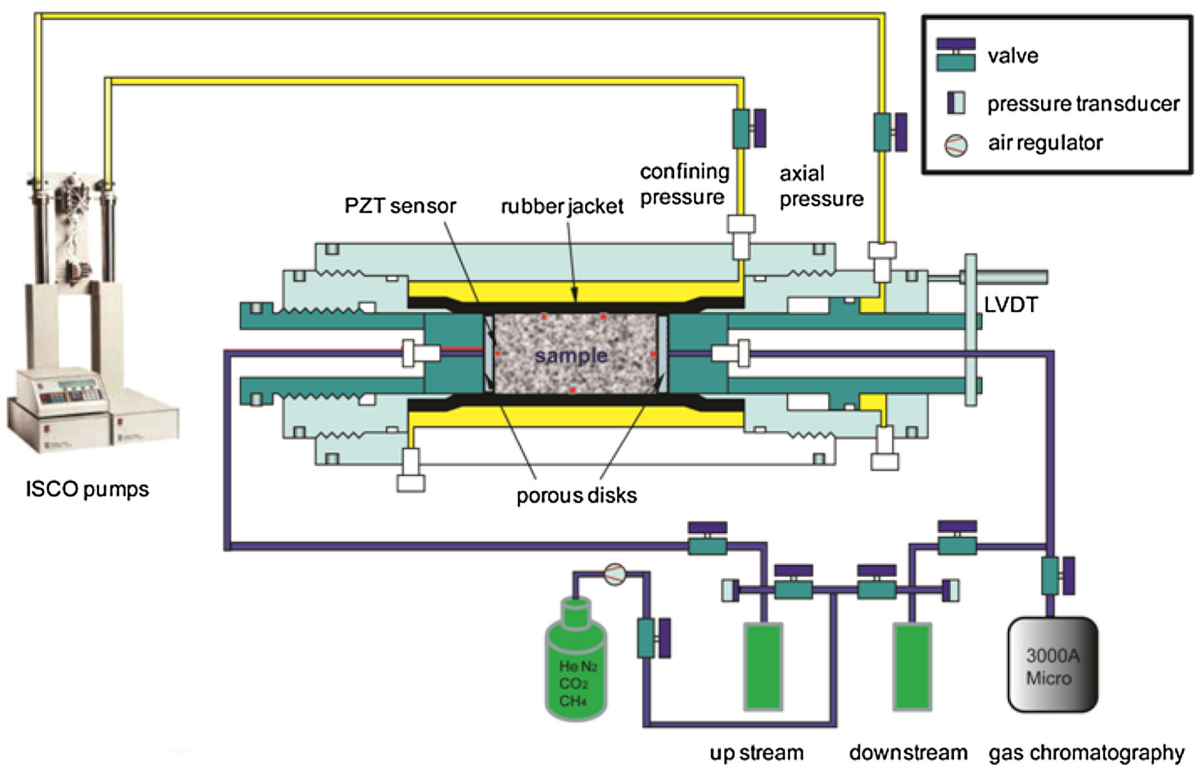

Fig. 2 Schematic of pulse test transient/hydraulic fracturing system (Wang et al. 2011). (ISCO pumps supply monitored confining and axial pressure; upstream reservoir supplies injection fluid and the fluid pressure is monitored; downstream is sealed at the *bottom* of the sample; sample is sealed with a rubber jacket and a porous disk/end plug is used to inject fluid into the sample. This set-up is also capable of acoustic emission and strain measurement as well as gas concentration measurement, however these features are not used in this study)

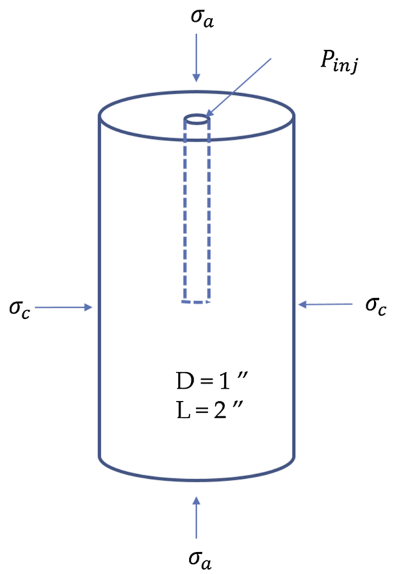

Fig. 3 Sample design

Calibration experiments are conducted with 27 samples of GRS to explore the effectiveness of the method of sealing the sample, especially with corrosive and low viscosity CO_2. Calibration experiments are performed with three methods of sealing (Fig. 4) to ensure congruent results—with the simplest and least invasive of the methods used for the experimental suite. The sealing methods are: (1) a platen with a single concentric O-ring encircling the central injection port (Fig. 4a) (2) a double O-ring design (Fig. 4b); and (3) use of a Swagelok fitting epoxied into the top borehole within the sample (Fig. 4c). Of these, the double O-ring design is the preferred method—simple and adequate. The single O-ring is an effective seal for H_2O but not for CO_2. The high pressure fitting is an effective but unnecessary seal compared to the dual O-ring design.

2.4 Standard experiment procedure

The jacketed sample is placed in the apparatus and axial and confining stresses are applied. Once at the desired pressure, the axial stress is held constant and the pump controlling the confining stress set to constant volume with a pressure relaxation of ~0.6 % which means during the experiment the confining stress can be decreased by ~0.6 % due to the instability of the pump. With confining stress set to constant volume, a rapid increase in confining pressure can also be used as a sign for sample failure. Fluid is then injected into the blind borehole at a constant flow rate (1 ml/min for H_2O; 5 ml/min for CO_2 and N_2). Breakdown in the sample is observed as a rapid drop in the borehole pressure and a simultaneous jump in the confining pressure (Fig. 5). This defines the breakdown pressure with a typical log shown in Fig. 5.

3 Results

Previous studies (Alpern et al. 2012; Gan et al. 2013) have shown that the breakdown pressures and morphology of induced fractures are dependent on both the fracturing fluid and the applied stress regime. We explore the mechanistic underpinnings of these

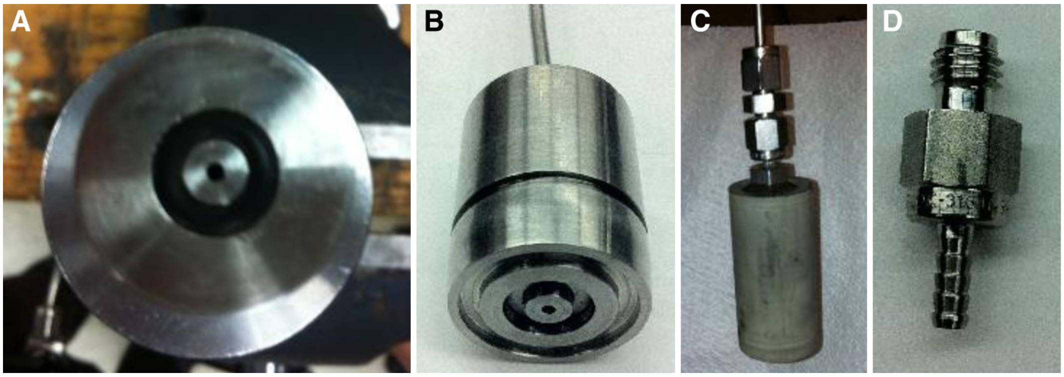

Fig. 4 Sealing methods: **a** Single O-ring seal within the platen; **b** Double O-ring seal; **c**: Fitting design; **d** Close-up of the fitting with barbs that are epoxied into the blind borehole within the sample

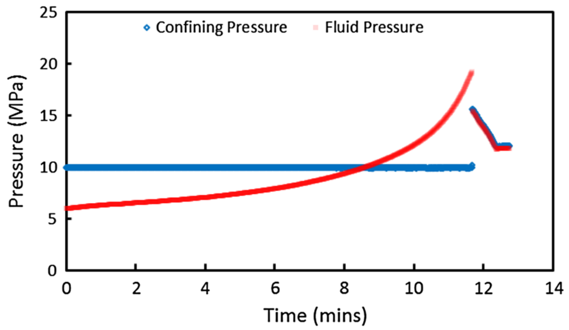

Fig. 5 Typical pressure response during an hydraulic fracturing experiment. (Sample: Green River shale; Stimulant: CO_2; Confining stress: 10 MPa; Axial stress: 20 MPa; Breakdown pressure: 19.3 MPa)

observations in the following, together with their consistency with the observed results in this study.

3.1 Theoretical considerations

Hydraulic fractures initiated from a cylindrical borehole in a simple-triaxial stress regime will open against the minimum principal stress (i.e. in the plane of the maximum principal stress). In our configuration, the fractures should develop either across the borehole (Fig. 6 left) when the axial stress is less than the confining stress, or along the borehole (Fig. 6 right) when the axial stress is the maximum stress.

When the axial stress is the maximum principal stress (Fig. 6 right), failure is based on the Hubbert and Willis (H–W) hydraulic fracturing criterion where the fracture evolves perpendicular to the local minimum principal stress at the borehole wall, when the rock tensile strength is exceeded. If there is no initial pore pressure in the rock, and assuming an elastic medium, the breakdown pressure is given by:

$$p_b = 3\sigma_{h_{min}} - \sigma_{h_{max}} + \sigma_t \tag{1}$$

where p_b is breakdown pressure, $\sigma_{h_{min}}$ is minimum horizontal stress and $\sigma_{h_{max}}$ is maximum horizontal stress (both perpendicular to the borehole), and σ_t is the tensile strength of the rock.

In our experiments, and for the specific case of the longitudinal fracture of Case 2 then $\sigma_{h\min} = \sigma_{h\max} = \sigma_c$ and the breakdown pressure is given by

$$p_b = 2\sigma_c + \sigma_t \tag{2}$$

where σ_c is the confining pressure ($\sigma_{min} = \sigma_{\max} = -\sigma_c$). Thus, for these cylindrical samples, the breakdown pressure should be solely a function of confining pressure for a defined tensile strength.

When the axial stress is the minimum principal stress (Fig. 6 left), the sample fails transversely to the borehole. In this case the stress concentration around the tip of the borehole is undefined at the sharp boundary of the borehole termination—acting as a

Fig. 6 Potential failure modes for different stress configurations

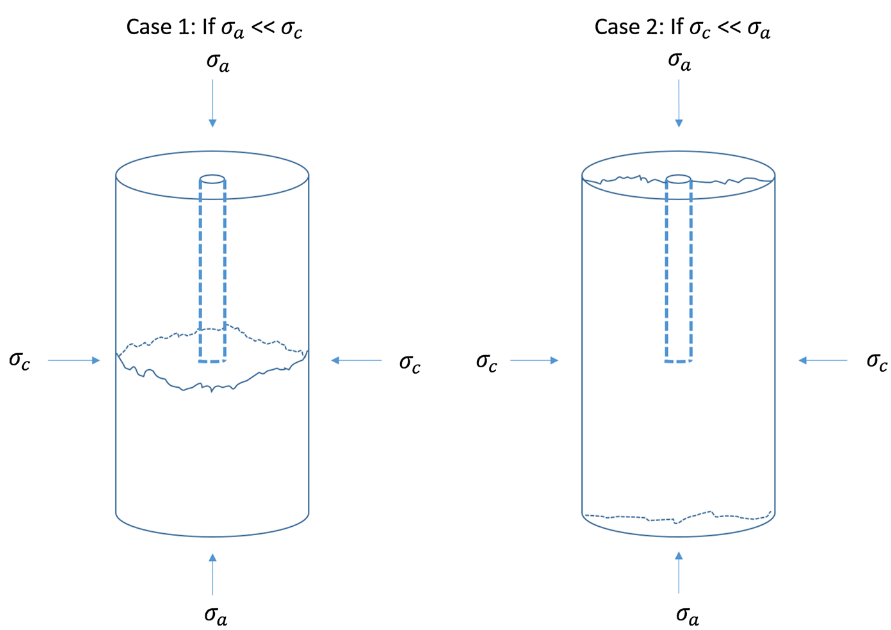

stress concentrator. Although theoretically undefined and large, it will be limited by blunting of the termination geometry and local failure. In this case the breakdown pressure may be defined generically as

$$p_b = A\sigma_a - B\sigma_C + C\sigma_t \tag{3}$$

where A, B and C are coefficients for axial stress, confining stress and tensile strength. Thus a similar arrangement may be applied to the H–W solution for a longitudinal fracture, with only the magnitudes of the coefficients A and B changing. Absent a stress concentration, the coefficients for Case 1 (when the confining stress is larger) would be $A = C = 1$ and $B = 0$, and for Case 2 (when the axial stress is larger), $A = 0$, $B = -2$, $C = 1$.

The results for the above equations are for the case that no fluid penetrates the borehole wall (Hubbert and Willis 1957). Where fluid penetration occurs, based on poroelastic theory considering the poroelastic stress induced by the fluid permeation into rocks (Haimson and Fairhurst 1967), the revised expression for both Cases 1 and 2 may be redefined as:

$$p_b = (A'\sigma_a + B'\sigma_c + C'\sigma_t)\frac{1}{1+\eta} \tag{4}$$

$$\eta = \frac{v\alpha}{(1-v)} \tag{5}$$

where A' is the coefficient for axial stress; B' is the coefficient for confining stress and C′ is the coefficient on the tensile strength (always unity); υ is the Poisson ratio and α is the Biot coefficient which reflects the poroelastic effect (Biot 1941); $\frac{1}{1+\eta}$ ranges between 0.5 (permeable, where fluid is allowed entry into the borehole wall with ŋ = 1, $\alpha = 1$ and $\upsilon = 0.5$) and 1 (impermeable, where fluid is excluded from the borehole wall with ŋ = 0 and $\alpha = 0$ which results in Eq. (4) collapsed into Eq. (3)).

Similar to the impermeable cases, when $\sigma_C < \sigma_a$ the coefficients $A' = 0$ and $B' = 2$ for longitudinal fracture (Case 2); when $\sigma_C > \sigma_a$ and neglecting the stress concentration effect, $A' = 1$ and $B' = 0$ for transverse fracture (Case 1).

3.2 Experimental results

A large number of experiments are completed on GRS under various stress conditions at ambient temperature. These experiments are completed for the three fracturing fluids H_2O, CO_2 (gas and liquid state) and N_2 (gas state). Results are grouped according to stress conditions and failure modes. For those failing longitudinally where the breakdown pressure is solely a function of confining stress and a given constant tensile strength, breakdown pressures are shown scaled with confining stress (Fig. 7).

Even though the results are somewhat scattered, the general trend is that CO_2 has larger breakdown pressures than N_2, which in turn has higher breakdown pressures than H_2O. If interpreted using the concepts (Eqs. 3–5) discussed previously, the magnitudes of the tensile strength are on the order of 4–10 MPa and the multiplier for the confining stress (B) is ~0.8–1.3. The Brazilian test also shows the tensile strength of GRS is ~10 MPa (Table 1).

When the samples fail in a transverse mode, ignoring the stress concentration effect, the breakdown pressure is principally controlled by axial stress. Breakdown pressures are shown as a function of axial stress in Fig. 8.

Again, the breakdown pressures are greatest for CO_2, lower for N_2 and lowest for H_2O. Projected tensile strength, is in the order of 12–20 MPa. The coefficient of the axial stress (A) is 0.7–1.2.

One thing to notice is that under a constant injection rate, the CO_2 pressure profile presents an extended plateau of constant pressure (Fig. 9b) due to condensation between ~5 and 7 MPa. This condensation period implies that the CO_2 transits from gas to liquid via a mixed-phase region. Due to the nature of the other fluids, this is not observed for H_2O and N_2 (Fig. 9).

3.3 Application to other rock types

Extensive attempts have been made to estimate the magnitude of wellbore breakdown pressure through analytical, semi-analytical and numerical approaches (Kutter 1970; Newman 1971; Tweed and Rooke 1973). The suitability of using GRS as an analog for other rock types may be established through comparison of index properties of strength, deformability, porosity and permeability, as well as organic content. These are given in Table 1. More specifically, direct scaling of fracture breakdown is possible when indices of extensional strength (tensile strength) and capillary behavior (scaled from permeability and porosity) are applied.

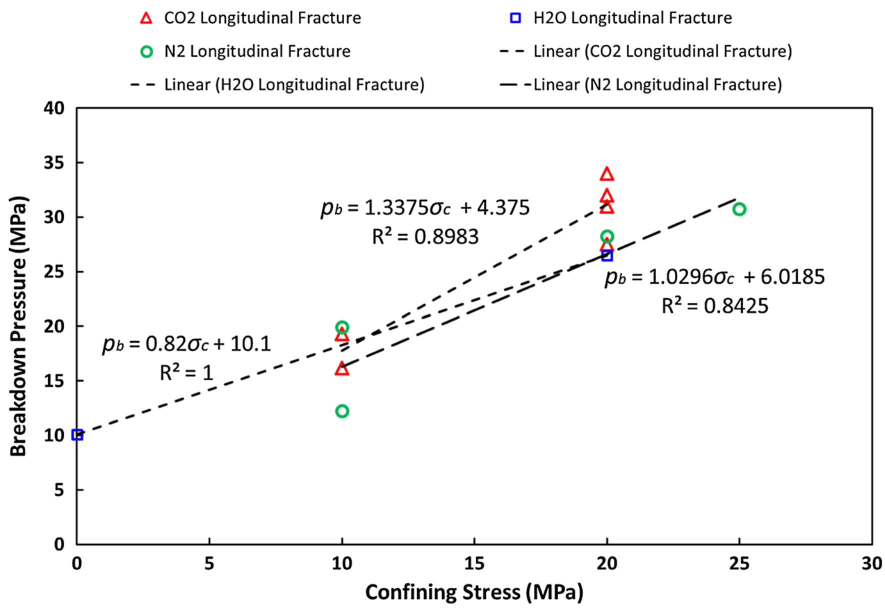

Fig. 7 Breakdown pressure as a function of confining stress (Case 2: longitudinal fracture)

The Green River shale is fine-grained, highly laminated, and with low-grade kerogen. Its geomechanical properties are shown in Table 1.

The various responses for breakdown for GRS in each of the configurations are:

Longitudinal fracture ($\sigma_{\min} = \sigma_c < \sigma_{axial}$):

$$CO_2: p_b = 1.34\ \sigma_{\min} + 4.4\ \text{MPa} \tag{6}$$

$$N_2: p_b = 1.04\ \sigma_{\min} + 6.0\ \text{MPa} \tag{7}$$

$$H_2O: p_b = 0.82\ \sigma_{\min} + 10.1\ \text{MPa} \tag{8}$$

Transverse fracture ($\sigma_{\min} = \sigma_{axial} < \sigma_c$):

$$CO_2: p_b = 1.18\ \sigma_{\min} + 11.8\ \text{MPa} \tag{9}$$

$$N_2: p_b = 0.66\ \sigma_{\min} + 19.7\ \text{MPa} \tag{10}$$

$$H_2O: p_b = 1.02\ \sigma_{\min} + 10.0\ \text{MPa} \tag{11}$$

A straightforward interpretation of these breakdown pressure estimates is that the stress offset is proportional or equal to the tensile strength. Further, the variation of the estimates with different confining

Table 1 Geomechanical properties of Green River shale

Rock type	GRS
Tensile strength, σ_T	9.3 MPa (load parallel to the bedding) (Li et al. 2015)
	13.4 MPa (load perpendicular to the bedding)
Young's Modulus, E	14.4 GPa
Permeability, k	$\sim 10^{-17}$ m^2 (Culp 2014)
Porosity, φ	$\sim$10 % (Morgan et al. 2002)
Bulk Modulus, K	3.5–5 GPa (Bulk modulus of Kerogen) (Yan and Han 2013)
	1.7–2.5 GPa (Shear modulus of Kerogen) (Yan and Han 2013)
Poisson ratio, v	0.2 (Aadnoy and Looyeh 2011)
Elastic moduli ratio, n	0.84 (Aadnoy and Looyeh 2011)
TOC	17–20 %

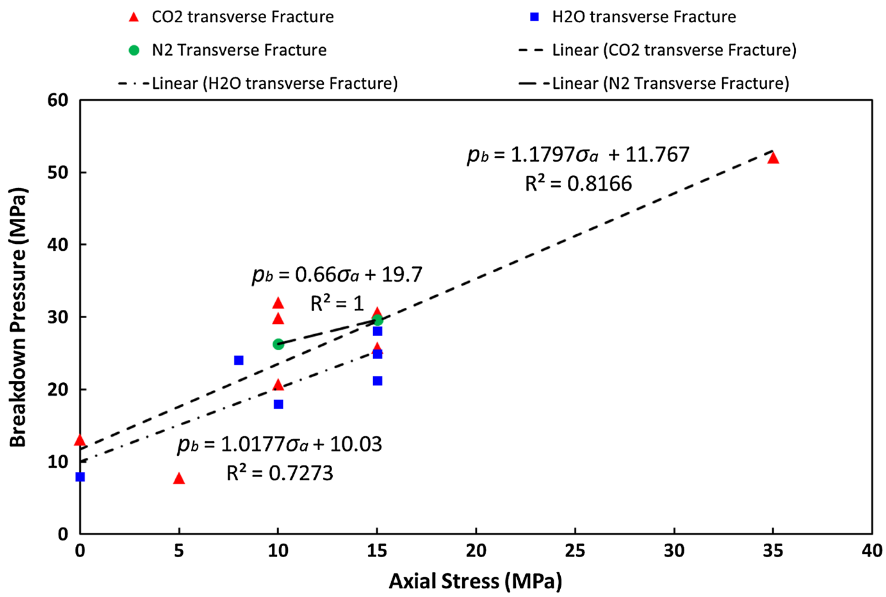

Fig. 8 Breakdown pressure as a function of axial stress (Case 1: transverse fracture)

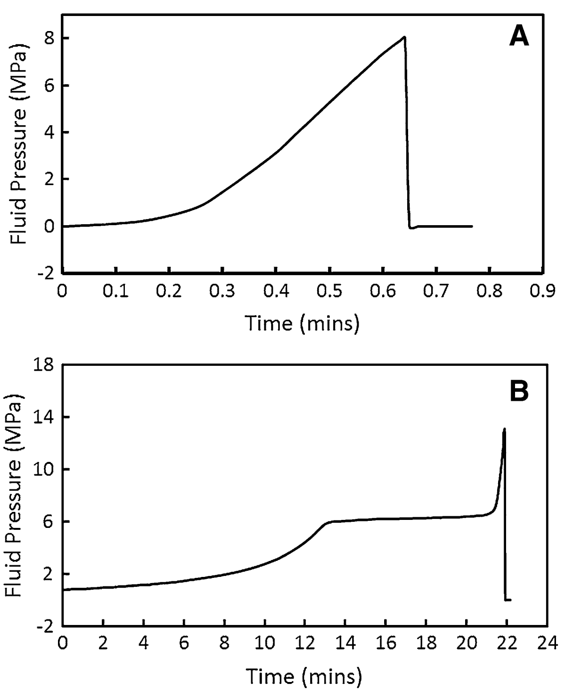

Fig. 9 Typical fluid pressure profiles for fracturing with **a** H_2O and **b** CO_2, which shows gas condensation behavior between ~5 and 7 MPa

or axial stresses are due to the stress regime and the stress concentrations around the borehole. Since the borehole configuration remains the same in all experiments, the results should therefore scale with confining stress and tensile strength.

3.4 Fracture surface morphology analysis

Fracture surfaces are measured using a Zygo New-View 7300 scanning white light interferometer with a scan speed up to 135 µm/s and a sub-nanometer resolution. Three samples are fractured with either H_2O, CO_2 or N_2, under a confining stress of 25 MPa and an axial stress of 15 MPa and breakdown pressures measured (Fig. 10). Only one fracture surface of the two halves of each sample is profiled since the fracture surface of the two halves are complementary. Three random spots with a 1.6 mm × 1.6 mm window are captured from the surface of each sample for measurement (Fig. 11).

3.4.1 Roughness

There are many different surface roughness parameters in use, although arithmetic average of the absolute values of the profile height deviations from the mean line, recorded within the evaluation length (S_a; Eq. 12) is the most common. Other common parameters include root mean square (RMS) S_q and the average distance between the highest peak and lowest valley in each sampling length (Eq. 15) S_z. RMS is the root mean square average of the profile height deviations

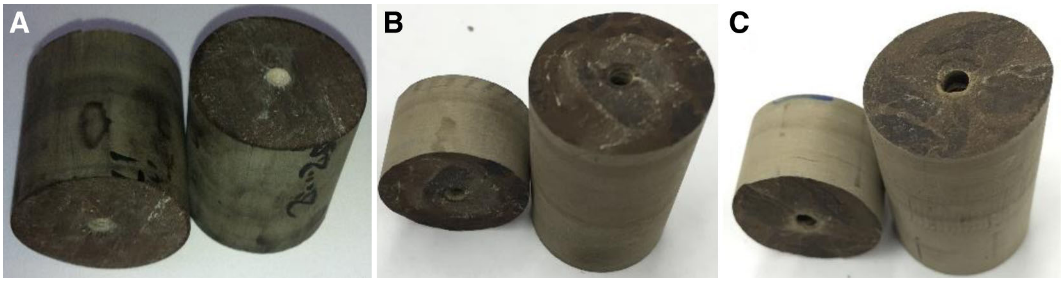

Fig. 10 Fracture patterns caused by **a**: H_2O; **b** CO_2; **c** N_2. (Sample: Green River shale; Confining stress: 25 MPa; Axial stress: 15 MPa)

from the mean line, recorded within the evaluation length (Eq. 13). Here fracture roughness is characterized by S_a, S_q and S_z

$$S_a = \frac{1}{n}\sum_{i=1}^{n}|y_i| \tag{12}$$

$$S_q = \sqrt{\frac{1}{n}\sum_{i=1}^{n}y_i^2} \tag{13}$$

$$S_t = S_p - S_v \tag{14}$$

$$S_Z = \frac{1}{l}\sum_{i=1}^{s}S_{t_i} \tag{15}$$

where the roughness profile contains n ordered, equally spaced points along the trace; y_i is the vertical distance from the mean line to the ith data point; S_p is the maximum peak height; S_v is the maximum valley depth; l is the number of sampling lengths; S_{t_i} is S_t for the ith sampling length.

The average S_a value for samples fractured with CO_2, H_2O and N_2 are 18.73, 11.04 and 8.79 microns, respectively. The average S_q value for CO_2, H_2O and N_2 are 22.94, 13.83 and 11.06 microns, respectively. In Fig. 12 the errors bars indicate the uncertainty of the experiment and variability of the data. Figure 12a, b show that there is a significant difference between: CO_2 versus H_2O; CO_2 versus N_2 but S_a and S_q are indistinguishable within the uncertainty interval between H_2O versus N_2.

The average S_z value for fracturing with CO_2, H_2O and N_2 hydraulic fracturing (HF) samples are 141.23, 103.39 and 87.77 microns. Figure 12c shows that there is a significant difference between: CO_2 versus N_2 but S_z is indistinguishable within the uncertainty interval between H_2O versus N_2; CO_2 versus H_2O.

Overall, the 2 figures above show that the HF surfaces for CO_2 have the highest roughness, followed by H_2O, and then N_2.

3.4.2 Complexity

Fracture complexity can be evaluated by considering the fractal dimension. The fractal characteristics of the artificial fractures has been investigated using the spectral method (Power and Durhum 1997), which describes the relation between the logarithms of power spectral density (PSD) and spatial frequency as linear for a fractal, with the slope of the line giveing the fractal dimension (Fig. 13). When the PSD of the surface heights $G(f)$ is given as a function of the spatial frequency f by

$$G(f) = Af^{-\alpha} \tag{16}$$

the fractal dimension of the surface ($1 < D < 2$) is determined by

$$D = \frac{5-\alpha}{2} \tag{17}$$

where α is the power in Eq. 16, determined from the slope of the log–log plot of $G(f)$. Therefore the fractal dimension of the fracture surface in Fig. 11 is determined to be 1.84, since α is 1.323.

The 1-D fractal dimension along the x and y direction of each measurement are shown in Table 2.

3.4.3 Other statistics

The mean and standard deviation of the distance away from the measuring mean plane are also calculated for statistic purpose. All of the fractures resulting from the three fracturing fluids have very similar mean values which is approximately zero (Table 3), and showing a

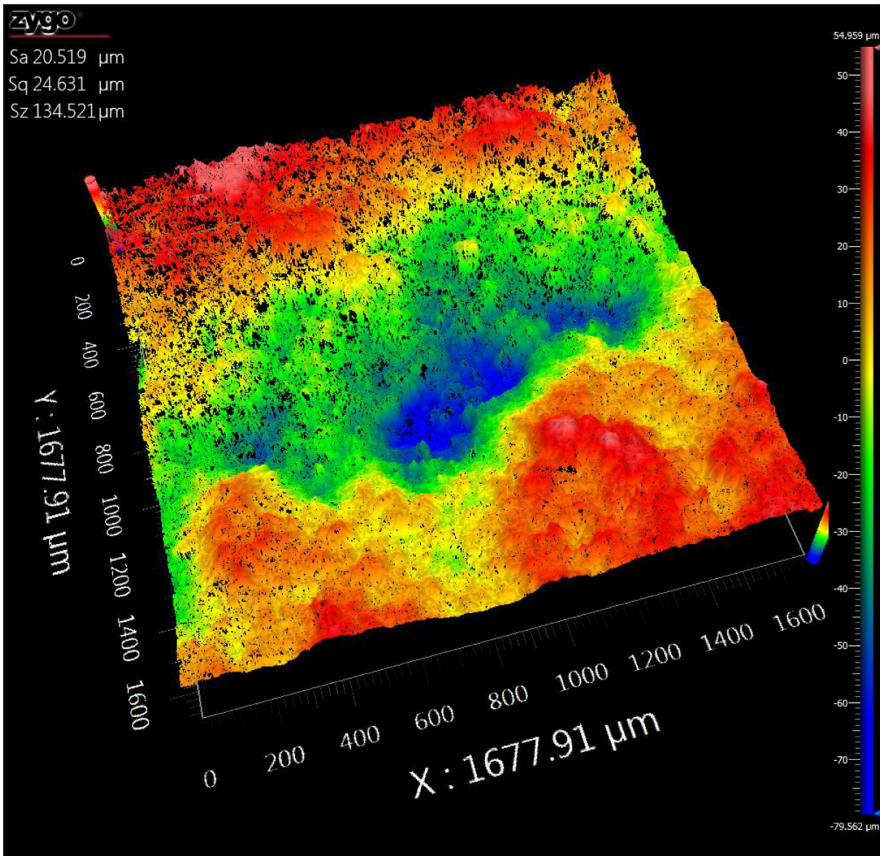

Fig. 11 The view of fracture surface on sample fractured with CO_2

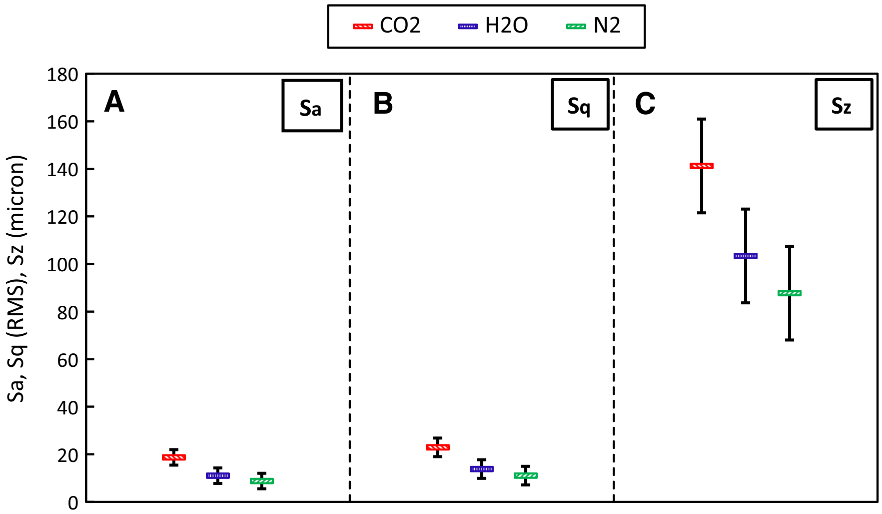

Fig. 12 S_a, S_q (RMS) and S_Z of fracture surface fractured with H_2O, CO_2 and N_2

normal distribution. However CO_2 has the highest standard deviation, indicating that the data points are spread out over a wider range of values, compared to H_2O and N_2 whose data points tend to be closer to the mean. These data also support that CO_2 HF surface is the most complex and roughest.

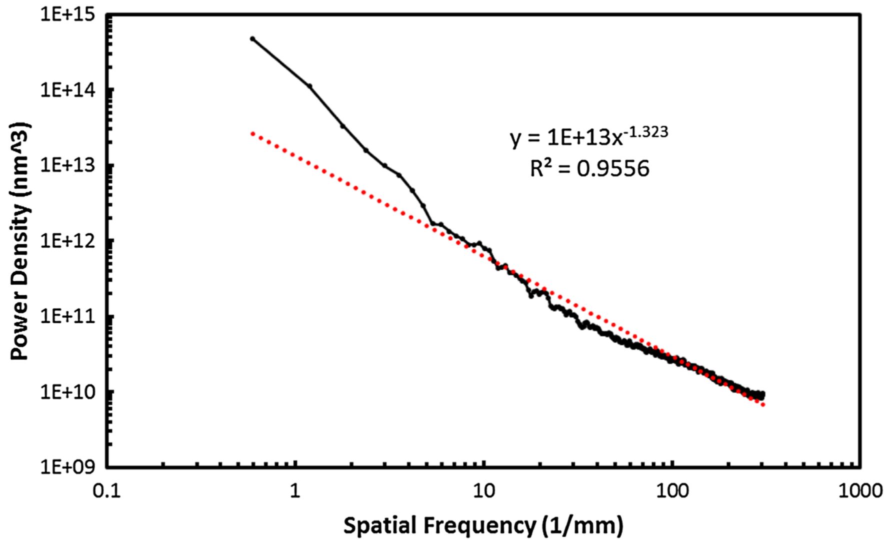

Fig. 13 Relationship between the logarithm of power spectral density and spatial frequency. (*CO_2* HF sample; #1 measurement; *x* direction)

Table 2 1-D fractal dimension along the *x* and *y* direction for each measurement

	CO_2	H_2O	N_2
Fractal dimension, $D_{1(x)}$	1.84–1.91	1.75−1.83	1.71–1.8
Fractal dimension, $D_{1(y)}$	1.77–1.85	1.8−1.84	1.73–1.81

Overall, *CO_2* HF surfaces have the highest fractal dimension, followed by *H_2O*, and then *N_2*. Hence, *CO_2* HF surfaces are the most complex ones, followed by *H_2O*, and then *N_2*

4 Discussion

A large number of experiments completed in Green River shale indicate the following:

1. Under the same applied stress conditions, *CO_2* returns the highest breakdown pressure, followed by *N_2*, and then *H_2O*. The distribution in breakdown pressures is of the order of ~25–~30 % of the maximum breakdown pressure for this progression of fluids from highest (with *CO_2*) to lowest (with *H_2O*). Under the same conditions of in situ rock stress and flow rate, *CO_2* has the higher breakdown pressure compared to *N_2*, possibly in part due to its higher viscosity (Ishida et al. 2012) and higher molecular weight (Alpern et al. 2012). In our study another reason for *CO_2* having higher breakdown pressure compared to *H_2O* could be attributed to higher flow rate (5 ml/min for *CO_2*; 1 ml/min for *H_2O*) of *CO_2* injection (Schmitt and Zoback 1993) (Garagash and Detournay 1997). For *CO_2* fracturing, the pore pressures cannot be recharged during the short time of the rapid pressurization with infiltration, placing the sample at a higher effective confining stress and making it both stiffer and more difficult to break. Since the initial pore pressure within the sample is zero in our experiments and the flow of fluid exerts an equivalent body force on the medium, the higher pore pressure gradient from the borehole wall to the outer boundary of the sample may result in larger induced compressive infiltration stresses at the borehole wall which must be overcome in order to initiate fracture. Lubinski (1954) suggests that the magnitude of the compressive stress produced by fluid

Table 3 The mean and standard deviation of the distance away from the measuring mean plane

	CO_2	H_2O	N_2
Mean (mm)	−0.00781 to −0.028342	−0.00752 to −0.01226	−0.03353 to 0.0033136
Standard Deviation	0.4784 to 0.79343	0.375587 to 0.52368	0.300645 to 0.505261

Detailed statistics of each measurement can be found in Table 4

Table 4 Statistics of each measurement

Parameter (unit)	CO_2			H_2O			N_2		
	#1	#2	#3	#1	#2	#3	#1	#2	#3
Sa (μm)	20.519	12.405	23.251	10.085	13.796	9.233	9.168	8.214	8.977
Sq (RMS) (μm)	24.631	15.488	28.705	12.369	17.611	11.496	11.310	10.586	11.294
Sz (μm)	134.521	110.942	178.226	96.894	125.042	88.225	72.992	75.678	114.626
Mode (mm)	12.249	3.410720	3.1729	−4.6531	4.6502	−0.9059	1.7671	−1.7399	1.1852
Median (mm)	2.83253	1.19189	0.4995	−0.2928	0.2737	0.41743	0.30731	−0.2264	0.038935
Mean (mm)	−0.028342	−0.00781	−0.02127	−0.01226	−0.00752	−0.01055	−0.03353	0.0033136	−0.026538
SD	0.596503	0.4784	0.79343	0.4371	0.52368	0.375587	0.300645	0.313302	0.505261
Fractal dimension, $D_{1(x)}$	1.84	1.86	1.91	1.79	1.83	1.75	1.77	1.8	1.71
Fractal dimension, $D_{1(y)}$	1.85	1.84	1.77	1.8	1.84	1.80	1.73	1.81	1.73

infiltration is directly in proportion to the difference between injection fluid pressure and far-field pore pressure (Eqs. 18, 19). The effect is similar to the temperature gradient on an elastic medium, as

$$\sigma_{fr} = (n-1)\beta\left(\frac{1-2\upsilon}{1-\upsilon}\right)\frac{1}{r^n}\int_{r_w}^{r}(p-\beta p_0)r^{n-1}dr \tag{18}$$

$$\beta = 1 - \frac{K}{K_m} \tag{19}$$

where σ_{fr} is the induced compressive infiltration stresses (also known as seepage stress); $n = 2$ (cylindrical flow) or 3 (spherical flow); β describes the compressibility of the material at some level; K is the bulk modulus of the porous material; K_m is the bulk modulus of the inter-pore material; υ is the Poisson's ratio; r is the current radial location; r_w is the wellbore radius; p is the pore pressure at a distance r away from the wellbore; p_0 is the far-field pore pressure. Therefore diminished pore pressures within the rock matrix results in higher compressive infiltration stresses which can act against, and therefore further postpone, fracture as observed for the CO_2 tests with fast injection rate.

A very subtle pore pressure drop (usually around 0.2–0.3 MPa) just before failure is observed in most of the CO_2 experiments, providing another piece of evidence for diminished pore pressure. This drop in pore pressure is known as "dilatancy hardening" in compressive failure tests (Brace and Martin III 1968) where it is defined as a consequence of new porosity produced in the irreversible damage of the rocks prior to failure. These slight drops in pore pressure before failure might indicate dilatancy of the rock occurred immediately prior to failure as well as increased permeability which possibly results from the production of dilatant porosity such that conductive paths within the rock structure are enhanced and fluid would be expected to flow into highly porous regions. Another possible reason for CO_2 having the highest breakdown pressure followed by N_2 and then H_2O could be stress corrosion (Anderson and Grew 1977). In this case, time-dependent chemical reactions aid in bond breaking near the initial crack tip. In our experiments, tensile failure of the samples typically take ~20 min for CO_2, ~12 min for N_2, and ~2 min for H_2O

2. Fracturing with CO_2, compared to other fracturing fluids, creates marginally more complex fracturing patterns (characterized by fractal dimension) as well as the roughest fracture surface (characterized by S_a, S_q and S_z) and with the greatest apparent local damage, followed by H_2O and then N_2. Study shows that low viscosity fluid tends to generate cracks extending more three dimensionally with a larger fractal dimension Ishida et al. (2004, 2012). This viscosity dependent behavior can be explained through the fluid loss equation, which indicates that a fracturing fluid with high viscosity results in a low rate of fluid-loss. Carter (1957) assumed that, for a fracture of uniform width that the fluid-loss velocity normal to the fracturing faces, v_l, takes the following form

$$v_l = \frac{K_l}{\sqrt{t - \tau}} \tag{20}$$

where v_l is the fluid-loss velocity; K_l is the overall fluid-loss coefficient and t is the current time; τ is the time when filtration starts. K_l includes three effects: (1) viscosity and relative-permeability effects of the fracturing fluid, (2) reservoir- fluid viscosity-compressibility effects, (3) wall-building effects. Howard and Fast (1957) proposed that the relation between K_l and viscosity is as following

$$K_l \propto \frac{1}{\sqrt{\mu}} \tag{21}$$

Thus fracturing fluid with high viscosity results in low fluid-loss rates and hence less leak-off from the generated fracture plane. Therefore the pressure in the produced facture can readily increase with the viscous fluid. Thus, the extension of a less complex fracture develops as a consequence,
Among these three fluids, N_2 has the smallest viscosity, followed by CO_2 and then H_2O. These considerations support well the observation of CO_2 HF surfaces being more complex than H_2O HF surfaces, but does not necessarily explain why N_2 HF surfaces are the least complex. Other literature also provides some other explanations that the geometry and dimensionality of some fractures may be a function of the fracture initiation point/borehole termination, failure pressure, and the physical characteristics of the testing material (Culp 2014).

3. Under a constant injection rate, the CO_2 pressure response shows a long plateau of constant pressure due to condensation between ~5 and 7 MPa. This condensation period implies the transit of CO_2 from gas to liquid through a mixed-phase region. Due to the features of the other fracturing fluid, this is not observed for H_2O and N_2.
4. There is a positive correlation between minimum principal stress and breakdown pressure for failure in both transverse fracturing (σ_3 *axial*) and longitudinal fracturing (σ_3 *radial*). CO_2 has the highest correlation coefficient/slope and H_2O has the lowest. This observation can be explained with the specific properties of the stimulating fluids and experiment conditions as illustrated in notation 1.

Acknowledgments This work was supported by Aramco Services. This support is gratefully acknowledged. We also thank Takuya Ishibashi for his assistance with fracture surface complexity measurement.

References

Aadnoy B, Looyeh R (2011) Petroleum rock mechanics: drilling operations and well design. June 9, 2011 ed. s.l., Gulf Professional Publishing

Alpern J et al (2012) Exploring the physicochemical processes that govern hydraulic fracture through laboratory experiments. In: 46th US symposium on rock mechanics and geomechanics

Anderson OL, Grew PC (1977) Stress corrosion theory of crack propagation with applications to geophysics. Rev Geophys Space Phys 15:77–104

Biot MA (1941) General theory of three-dimensional consolidation. J Appl Phys 12(2):155–164

Brace WF, Martin RJ III (1968) A test of the law of effective stress for crystalline rocks of low porosity. Int J Rock Mech Min Sci Geomech Abstr 5:415–426

Bullis K (2013) Skipping the water in fracking-the push to extend fracking to arid regions is drawing attention to water-free techniques. [Online] Available at: http://www.technologyreview.com/news/512656/skipping-the-water-in-fracking/. Accessed 22nd Feb 2015

Carter RD (1957) Appendix to ‘‘optimum fluid characteristics for fracturing extension’’. In: Howard GC, Fast CR (eds) Drilling and production practice, volume API, p 267
Culp B (2014) Impact of CO_2 on fracture complexity when used as a fracture fluid in rock. In: A thesis in geoscience
Faraj B, Brown M (2010) Key attributes of Canadian and US productive shales: scale and variability. In: AAPG annual convention, New Orleans
Friehauf KE (2009) Simulation and design of energized hydraulic fractures. UT Austion Doctor of Philosophy Dissertation
Friehauf KE, Sharma MM (2009) Fluid selection for energized hydraulic fractures. In: SPE annual technical conference and exhibition, New Orleans
Gan Q et al (2013) Breakdown pressures due to infiltration and exclusion in finite length boreholes. In: 47th US symposium on rock mechanics and geomechanics
Garagash D, Detournay E (1997) An analysis of the influence of the pressurization rate on the borehole breakdown pressure. Int J Solids Struct 34(24):3099–3118
Gupta SD et al (2009) Development and field application of a low pH, efficient fracturing fluid for tight gas fields in the greater Green River Basin, Wyoming. In: SPE production and operations 24(04): 602–610
Haimson B, Fairhurst C (1967) Initiation and extension of hydraulic fractures in rocks. In: SPE, pp 310–318
Hall R, Chen Y, Pope TL, Lee JC (2005) Novel CO_2-emulsified viscoelastic surfactant fracturing fluid system. In: SPE annual technical conference and exhibition, Dallas
Howard GC, Fast CR (1957) Optimum fluid characteristics for fracturing extension. In: Drilling and production practice, pp 261–270
Hubbert MK, Willis DG (1957) Mechanics of hydraulic fracturing. In: Transactions of Society of petroleum engineers of AIME, volume 210, pp 153–168
Ishida T, Chen Q, Mizuta Y, Roegiers JC (2004) Influence of fluid viscosity on the hydraulic fracturing mechanism. J Energy Resour Technol 126:190–200
Ishida T et al (2012) Acoustic emission monitoring of hydraulic fracturing laboratory experiment with supercritical and liquid CO_2. Geophys Res Lett 39(16):1–6
King GE (2010) Thirty years of gas shale fracturing: what have we learned? In: SPE annual technical conference and exhibition, Florence
Kutter HK (1970) Stress analysis of a pressurized circular hole with radial cracks in an infinite elastic plate. Int J Fract 6:233–247
Li X et al (2015) Hydraulic fracturing in Shale with H2O, CO2 and N2. In: San Francisco, 49th US rock mechanics/geomechanics symposium
Lubinski A (1954) The theory of elasticity for porous bodies displaying a strong pore structure. In: Proceedings of 2nd US Natlional Congress Applied Mechanics, pp 247–256
Morgan CD et al (2002) Characterization of oil reservoirs in the lower and middle members of the Green River formation, Southwest Uinta Basin, Utah. Wyoming, AAPG Rocky Mountain Section Meeting AAPG Rocky Mountain Section Meeting
Newman JC (1971) An improved method of collocation for the stress analysis of cracked plates with various shaped boundaries. NASA TN, pp 1–45
Power WL, Durhum WB (1997) Topography of natural and artificial fractures in granitic rocks: implications for studies of rock friction and fluid migration. Int J Rock Mech Min Sci 34(6):979–989
Schmitt DR, Zoback MD (1993) Infiltration effects in the tensile rupture of thin walled cylinders of glass and granite: implications for the hydraulic fracturing breakdown equation. Int J Rock Mech Min Sci Geomech Abstr 30:289–303
Tweed J, Rooke DP (1973) The distribution of stress near the tip of a radical crack at the edge of a circular hole. Int J Eng Sci 11:1185–1195
Vincent MC (2010) Refracs: Why do they work, and why do they fail in 100 published field studies? In: SPE annual technical conference and exhibition, Florence
Wang S, Elsworth D, Liu J (2011) Permeability evolution in fractured coal: the roles of fracture geometry and water-content. Int J Coal Geol 87:13–25
Yan F, Han D-H (2013) Measurement of elastic properties of kerogen. In: SEG Houston 2013 Annual Meeting, Houston